Discriminating Underwater LiDAR Target Signatures using Sparse Multi-spectral Depth Codes

Puneet S Chhabra*, Aurora Maccarone, Aongus McCarthy, Andrew M Wallace and Gerald S Buller
School of Engineering and Physical Sciences, Heriot Watt University, Edinburgh, EH14 4AS

***Abstract*—The analysis and discrimination of underwater multi-spectral full-waveform LiDAR signatures acquired using a single-photon counting sensor is presented. We use a realistic scaled exemplar of a marine environment, with known and unknown targets, and show how we can both discriminate different materials and detect and locate mines. Each waveform is a temporal photon histogram whose inherent nature changes with the laser wavelength, target geometry and environment. Discriminatory dictionaries for target materials and mine types are learnt by making multi-spectral measurements. An accuracy of 97.8% and 98.7% was achieved for material and mine type discrimination, respectively.**

***Index Terms*—Photon counting, dictionary learning, multi-spectral, lidar, ATR, full-waveform, target discrimination**

I. Introduction

Terrestrial and aerial light detection and ranging (LiDAR) has enabled researchers to explore the third dimension, *depth*; this has advantages in remote sensing [1], bathymetric mapping [2], defence and security [3], and restoration and archaeology [4]. It is only recently that LiDAR systems have been built and tested for underwater applications. Commercial and academic focus [2] on bathymetric LiDAR has been on shallow waters and uses either monochromatic laser sources or a maximum of two wavelengths. This work is the first to report signal analysis and discrimination of underwater LiDAR data for mine counter-measures (MCM).

The multi-spectral depth imaging system [5] used in this study is based on the time-of-flight (ToF) approach using time-correlated single photon counting (TCSPC). Figure 1a illustrates a schematic of the experimental set-up. The TCSPC module (Hydraharp in Figure 2) time-stamps each photon event reflecting from a target and records it using a single-photon detector. The photon counts can then be time gated to form a histogram, a *full-waveform*, whose inherent nature depends on several factors, e.g., the laser wavelength, surface geometry and transmission medium. Figure 1b illustrates an *exemplar* used in this paper which has several targets embedded in a sand-cement-epoxy mixture, and was imaged in a tank filled with clear unfiltered tap water. Making such measurements is the first step to demonstrate how LiDAR could be used as an alternative to acoustic sensors for MCM purposes in very challenging environments.

*As a joint PhD candidate P. S. Chhabra is also with the University of Edinburgh. Correspondence: psc31@hw.ac.uk

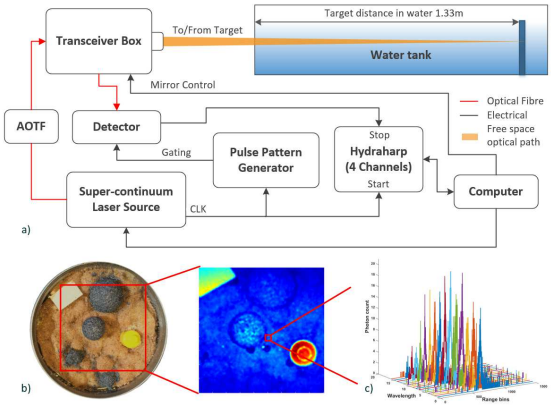

Fig. 1: a) A schematic of the experimental set-up; b) (left) an exemplar under investigation with different targets; (middle) Amplitude image, colour coded photon count, blue (low) to red (high) c) 16 full LiDAR waveforms at different wavelengths for a single pixel.

A. Contributions & Outline

The main contribution of this work is a novel approach to discriminate target signatures acquired by an underwater multi-spectral LiDAR system. This has been applied to identify both materials and specific targets for MCM.

In Section II we describe the basis of our approach, including firstly i) a "reflectance" aware spectral depth representation (SDR); and, secondly ii) a semi-supervised discriminatory objective function as an enhancement to the traditional sparse approximation scheme. In Section III we describe our implementation of the earlier theory, giving pseudocode descriptions of our software. The evaluation of the method on our own experimental data is given in Section IV. Finally, our conclusions are presented in Section V.

B. Experimental Setup

The experimental set-up is illustrated in Figure 1. Table I summarises the sensor equipment and acquisition parameters used. The exemplar was lowered underwater and kept at a distance of 1.33m from the SPC sensor. In order to limit the influence of any ambient illumination, the experiment was carried out in a dark room. The instrumental response was measured using a reference scatterer, a Spectralon panel, which was placed approximately at normal incidence to the beam. For

TABLE I: Experiment Key Parameters

Parameter	Value
Environment	Clear unfiltered tap water
Laser System	NKT Photonics supercontinuum laser source and tunable filter fibre-coupled to the transceiver unit
Illuminating Wavelength	500nm - 725nm
Laser Beam Diameter	$\approx 300\mu m$
Laser Repetition Rate	19.5MHz
Acquisition Mode	Exemplar 1: 200 x 200 pixels Area: $5cm$ x $5cm$ Pixel acquisition time: 10ms
Histogram bin width	2ps
Histogram Length	4500 bins (after gating)
Avg. Optical Power	$\approx$ 300nW

each pixel a 4500 bin time-gated histogram is created with a depth resolution of $300\mu m$, which is referred to as, *Single Photon Counting* data in Figure 2. Such measurements are repeated for 16 wavelengths ranging between 500nm to 725nm, equally spaced by 15nm. The choice of the wavelengths hinges on a detailed, previous study [5].

II. The Proposed Approach - An Overview

The proposed approach summarised in Figure 2 has three main stages: i) spectral depth representation (SDR) (see Section II-A, where a representation based on the LiDAR equations and surface geometry is proposed; ii) signal approximation and discrimination (SAD) to create and learn spectral sparse codes of the representations produced in stage 1, Section III; and, iii) prediction where unseen target signatures are classified.

A. Stage 1 - Spectral Depth Representation

The following assumptions were made when processing raw multi-spectral SPC data: i) one peak per waveform was extracted at each wavelength; ii) SPC waveforms are aligned and normalised with respect to the Spectralon target, with 10% reflectance; iii) the laser beam width is less than surface differential. For a beam width of $300\,\mu m$, the smallest target diameter under-investigation was around $0.5\,cm$. Finally, iv) a fixed stand-off distance from the sensor is assumed and the sensor is stationary.

1) Spectral FW-LiDAR Features: In previous work for the analysis of urban and forest scenes using laser scanning, several classification and feature relevance algorithms [1], [6] have been proposed. However, these methods do not truly embed the full-waveform properties and the spectral reflectance of the observed objects. Our SDR representation captures such variations from the waveform and the point cloud data. For N acquired sets of waveforms at Λ wavelengths, $N \times \Lambda$ waveforms are processed and the echo properties are extracted, Eq. 2. The transmitted time signature of the super-continuum laser source is an exponential pulse and the degree of modulation on the backscattering beam depends on the surface geometry

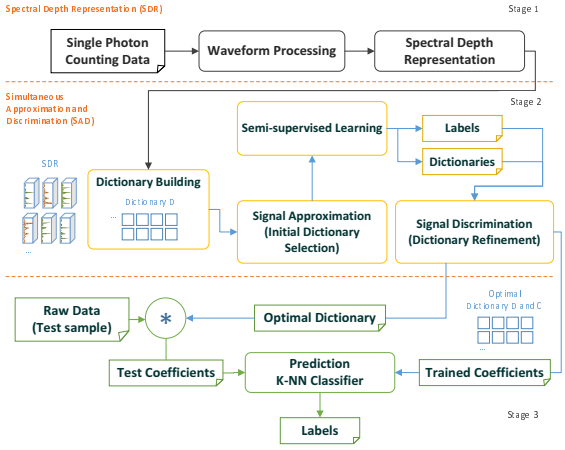

Fig. 2: The Proposed Approach.

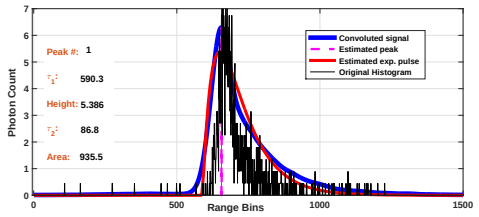

Fig. 3: An exponential pulse and a least-square fit to a returning target signature for a single wavelength.

and its spectral reflectance. Figure 3 illustrates one such return as a black curve. The pulse has the form

$$f(t) = k\left(e^{-t\mathcal{T}_1} - e^{-t\mathcal{T}_2}\right), \quad (t \geqslant 0),$$
$$\text{where, } k = \frac{\mathcal{T}_2 e^{(t_p - t_0)\mathcal{T}_1}}{(\mathcal{T}_2 - \mathcal{T}_1)}, \text{and} \quad t_p = \frac{\ln(\mathcal{T}_2/\mathcal{T}_1)}{(\mathcal{T}_2 - \mathcal{T}_1)} \tag{1}$$

The waveform processing module, stage 1 of Figure 2, finds the location within in each waveform where the average curvature, controlled by a specified region, is concave down, t_0. Once this location is identified, a least-square fit of a double exponential pulse provides the true position, the temporal parameters, $\mathcal{T}_1$, $\mathcal{T}_2$ and the area under the curve, A_λ. Figure 3 shows how an exponential pulse was fitted, the pink curve, to the incoming full-waveform, the black curve. The parameters $\mathcal{T}_1$ and $\mathcal{T}_2$, represent the fall and the rise of the exponential pulse respectively. These are computed at each wavelength.

2) Depth Representation (DR): The FW processing leads to a dense 3D point cloud. In order to capture local surface variations, a regional variance-covariance matrix was computed on the 3D point cloud. The radius, r, of the region shown in Figure 4 can be altered depending on the point cloud density. West et al. [6] show how Eigenvalues can be used to describe the local, spatial distribution of the 3D point cloud. They compute discrete moments within a neighbourhood that can describe the planarity, linearity, sphericity and anisotropy.

Table II illustrates how these properties are computed, provided the Eigenvalues $\mathcal{E}_1 > \mathcal{E}_2 > \mathcal{E}_3$. The Eigenvalues

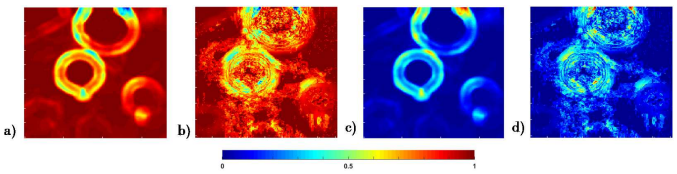

Fig. 4: Raster images of different geometric features computed for each 3D point, controlled using a local neighbourhood radius, r. (a) Anisotropy $A_{\mathcal{E}}$, b) Planarity $P_{\mathcal{E}}$, c) Sphericity $S_{\mathcal{E}}$ and d) Linearity $L_{\mathcal{E}}$ Table II.

TABLE II: Depth Representations using Eigenvalues

Linearity $L_{\mathcal{E}}$	$\frac{\varepsilon_1-\varepsilon_2}{\varepsilon_1}$	Sphericity $S_{\mathcal{E}}$	$\frac{\varepsilon_3}{\varepsilon_1}$
Planarity $P_{\mathcal{E}}$	$\frac{\varepsilon_2-\varepsilon_3}{\varepsilon_1}$	Anisotropy $A_{\mathcal{E}}$	$\frac{\varepsilon_1-\varepsilon_3}{\varepsilon_1}$

computed are invariant to 3D rotation [6] and view-point since they are computed locally. Four local 3D surface features, Anisotropy, $A_{\mathcal{E}}$, Planarity, $P_{\mathcal{E}}$, Sphericity, $S_{\mathcal{E}}$ and Linearity, $L_{\mathcal{E}}$ are computed within a neighbourhood, governed by radius r, of each 3D point. Finally, the depth D_z per pixel completes the SDR vector. A combined per-pixel representation was then fed into the stage 2 of the approach, the SAD. For each pixel, the SDR representation is a vector of 53 elements. For the experiments reported here, $\Lambda = 16$. Set one (elements 1 to 16) corresponds to the $\mathcal{T}_1$, set two (elements 17 to 32) corresponds to the $\mathcal{T}_2$, set three (elements 33 to 48) corresponds to A_λ. The remaining elements are the local geometric properties. So the final representation looks like

$$F_v = \Big[\{\mathcal{T}_{1,\lambda}\}_{\lambda=1}^{\Lambda}, \{\mathcal{T}_{2,\lambda}\}_{\lambda=1}^{\Lambda}, \{A_\lambda\}_{\lambda=1}^{\Lambda}, A_{\mathcal{E}}, P_{\mathcal{E}}, S_{\mathcal{E}}, L_{\mathcal{E}}, D_z\Big] \quad (2)$$

B. Stage 2 - Signal Approximation and Discrimination

Signal representation has a significant impact on the discriminatory nature of any classification system. Over the years, research in image characterisation has provided many compact and invariant representations e.g., image saliency, edge detections, bags-of-features (BoF) [7]. The BoF approach uses a vector quantisation (VQ) scheme in order to encode relationships between high-dimensional image patches belonging to the same class. In [7], VQ was applied to local regional histograms in order to generate cluster means. Cluster membership can be controlled in the higher-dimensional space and distance measures can be computed. The VQ scheme forces a cardinality constraint on cluster membership leading to a coarse representation of the input signal. This work proposes an alternative to the VQ scheme and not only relaxes the cardinality constraint but also improves the discriminatory capabilities. For completeness, first a short overview of the VQ method is presented in Section II-B1 followed by the proposed alternative formulation in Section II-B2.

1) Vector Quantisation: Let $\mathbf{W}$ be a set of SDR in a P-dimensional space, i.e., $\mathbf{W} = [w_1, ..., w_{\mathrm{N}}]^T \in \mathbb{R}^{\mathrm{N}\times\mathrm{P}}$. The VQ scheme applies a K-means clustering algorithm to solve the following problem

$$\arg\min_{\mathbf{Q},\mathbf{Z}} \sum_{n=1}^{N} ||w_n - q_n\mathbf{Z}||_2^2,\ Card\,(q_n) = 1, \quad |q_n| = 1, q_n \geqslant 0\,, \forall n, \quad (3)$$

where, $\mathbf{Z} = [z_1, ..., z_K]^T \in \mathbb{R}^{\mathrm{P}\times\mathrm{K}}$, are the K cluster centres, a *codebook* are unknown. $||.||_2^2$ and $|.|$ denotes the squared L_2 and L_1 norm, respectively. The cluster membership in Eq. (3) can be written as $\mathbf{Q} = [q_1, ..., q_N]^T$.

2) Discriminatory Sparse Codes: An alternative to a restrictive VQ approach is to relax the $Card\,(q_n)$ constraint to allow more than 1 non-zero element. In this work the traditional sparse approximation scheme was modified and a new discriminatory objective function was added. Suppose we have access to the best $\mathbf{Z}$, the new modified SAD problem can be written as

$$\arg\min_{\mathbf{Q},\mathbf{Z}} \left[\beta_2 \sum_{n=1}^{\mathrm{N}} ||w_n - q_n\mathbf{Z}||_2^2 + \beta_1 \sum_{n=1}^{\mathrm{N}} |q_n| + G\,(\mathbf{Q})\right], \quad \text{subject to}\, |q_n| \leqslant 1,\ \forall n = 1, 2, ..., N \quad (4)$$

In Eq. 4, the codebook $\mathbf{Z}$ is an *overcomplete* basis set, a *dictionary*, where $\mathrm{K} \gg \mathrm{P}$. The term $G\,(\mathbf{Q})$ is a discriminatory function that minimises inter-class and maximises intra-class variance. Detailed explanation of $G\,(\mathbf{Q})$ and step by step implementation of SAD is given in Section III. The penalising terms, β_1 and β_2 control the importance of the sparsity constraint and the reconstruction error, respectively.

The solution to (4) can be divided in to two steps: i) solve Eq. (4) with respect to $\mathbf{Q}$ and $\mathbf{Z}$. The dictionary, i.e, codebook, $\mathbf{Z}$ and coefficients $\mathbf{Q}$ are retained; ii) for a test signal, the coefficients are obtained by optimising Eq. (4) with respect to $\mathbf{Q}$ only. The individual functional blocks within each stage are explained in detail below along with their implementation details.

The discriminative nature of Eq. 4, $\mathrm{G}\,(\mathbf{Q})$ is expressed below. For a set of coefficients $\mathbf{Q} = [q_1, q_2, ..., q_{\mathrm{K}}]$, where $q_1, ..., q_k, ..., q_{\mathrm{K}}$ are the coefficients for the dictionary *atoms*, of which K_c samples are in class Ω_c, for $1 \leqslant c \leqslant \Omega$, the mean and variance for class Ω_c can be defined as:

$$\mu_c = \frac{1}{\mathrm{K}_c} \sum_{q\,\in\,\Omega_c} q\,; \quad \upsilon_c^2 = \frac{1}{\mathrm{K}_c} \sum_{z\,\in\Omega_c} ||z - \mu_c||_2^2 \quad (5)$$

The mean of all coefficient samples can be written as:

$$\mu = \tfrac{1}{\mathrm{K}} \textstyle\sum_{k=1}^{\mathrm{K}} q_k. \quad (6)$$

The *inter-class* scatter matrix, S_w and the *intra-class* scatter matrix, S_b can be defined as:

$$S_b = || \sum_{c=1}^{\Omega} \mathrm{K}_c\,(\mu_c - \mu)\ (\mu_c - \mu)^T\ ||_2^2\,; \quad S_w = \sum_{c=1}^{\Omega} \upsilon_c^2 \quad (7)$$

Finally, the Fisher discrimination function is defined as:

$$\mathrm{G}\left(\mathbf{Q}\right) = S_w^{-1} S_b, \tag{8}$$

Using Eq. (5) - (8), Eq. 4 can be solved using an orthogonal matching pursuit (OMP) algorithm [8]. The modified version, simultaneous approximation and discrimination (SAD) was presented in [3]. Algorithm 2 presents step by step details to solve Eq. 4.

III. Implementation Details - Pseudocode

In this section, the solution to Eq. (4) along with details of the discriminatory function $G(\mathbf{Q})$ is presented. First, the sparse codes for the SDR, from stage 1, are generated and a dictionary and their respective coefficients are learnt. Further, with the help of a semi-supervised clustering approach, these sparse codes are optimised for maximum discrimination. The pseudo-code to the approach in Figure 2 is presented in Algorithm 1.

A. Stage I - Lines 1 to 11

For a given set of input pixels, $\mathbf{W} \in \mathbb{R}^{\mathrm{N}}$, the aim is to create a representation that has a physical basis, LiDAR equations and target geometry. Lines 1 - 11 of Algorithm 1 generate a P-dimensional representation $\mathbf{F} \in \mathbb{R}^{(\mathrm{N}\times\Lambda)\times\mathrm{P}}$. In total, 40,000 waveforms were recorded for 16 different wavelengths. Lines 3 and 4 process each pixel for 16 different wavelengths. Lines 4 - 7 correct the intensity at each wavelength. For each pixel, line 7 aligns the 16 waveforms with respect to the system impulse, measurements made on a Spectralon target in advance and estimates the depth, point cloud matrix $\mathbf{P}$. Finally, line 10 compute the FW properties and geometric shape properties, as explained in Section II-A.

B. Stage II and III- Lines 12 to 21

Given a $\mathbf{F} \in \mathbb{R}^{(\mathrm{N}\times\Lambda)\times\mathrm{P}}$ matrix, the aim is to produce a set of sparse codes that are optimal and highly discriminatory, especially in identifying different materials. From a partially labelled set, U, line 13 selects a small sub-set, K, of representations, where $\mathrm{K} \gg \mathrm{P}$, and initialises them to $\mathbf{Z}$. Equation 4 is solved for $\mathbf{Q}$ and $\mathbf{Z}$ but without the optimisation add-on $G\left(\mathbf{Q}\right)$, Eq. 8. Solving Eq. 4 with the discriminatory function, $G\left(\mathbf{Q}\right)$ produces $\mathbf{Q}$ and $\mathbf{Z}$ that maximises the intra-class variance and minimises the inter-class variance. A semi-supervised approach can be adopted here, where labels are generated by clustering $\mathbf{Q}$ into three different clusters.

IV. Results and Analysis

The discriminatry performance of our approach is analysed using the exemplar of Figure 1a. Two sets of experiments were carried out: i) *Material Discrimination*: classify target signatures into three constituent materials, *sand*, *plastic* and *metal*, used to make the exemplar; ii) *Mine Discrimination*: classify different mine types, which not only differ in shape but also in material. Four different mines were used, *Plastic 1*, a cuboid shaped mine, *Plastic 2*, a spherical shaped mine, *Metal 1* and *Metal 2*, small and large spherical shaped metallic mines, respectively.

Input: SPC data $\mathbf{W} \in \mathbb{R}^{\mathrm{N}\times\Lambda}$, Partial labelled set, Ω
Output: Dictionary $\mathbf{Z}$, Coefficients $\mathbf{Q}$ and pixel labels
// **Stage I - SDR. See Section II-A**
1 **begin**
2 SDR matrix $\mathbf{F} \leftarrow [\,]$
3 **forall the** $n \in [1, \mathrm{N}]$ **do**
4 **forall the** $\lambda \in [1, \Lambda]$ **do**
5 CorrectIntensity$\left(w_{n,\lambda}, s_\lambda\right)$
6 **end**
7 $\mathbf{W}_{align} \leftarrow$ AlignWaveforms$\left(\{w_{n,\lambda}\}_{\lambda=1}^{\Lambda}\right)$
8 $\mathbf{P} \leftarrow$ EstimateDepth$(\mathbf{W}_{align})$
9 **end**
10 $\mathbf{F} \leftarrow$ SDR$\left(\mathbf{W}_{align}, \mathbf{P}\right)$ // Eq. 2
11 **end**
// **Stage II - SAD. See Section III-B**
12 **begin**
// Get ω random SDR's from set Ω
13 $\omega \in \mathrm{R}^{\mathrm{K}} \leftarrow$ Randperm$\left(\Omega\right)$, where $\mathrm{K} \gg \mathrm{P}$
$[\mathbf{Q}_{init}, \mathbf{Z}_{init}] \leftarrow$ Solve Eq. (4) without $G\left(\mathbf{Q}\right)$
14 $classIdx \leftarrow \mathrm{VQ}\left(\mathbf{Q}, \omega\right)$ // Eq. 3
// Dictionary selection. Algorithm 2
15 $[\mathbf{Q}, \mathbf{Z}, dictIdx] \leftarrow \mathrm{SAD}\left(\mathbf{F}, \mathbf{Z}_{init}, classIdx, param\right)$
// Reorder dictionary indices
16 $\mathbf{Z}_{opt} \leftarrow$ Reorder$\left(\mathbf{Z}, dictIdx\right)$
17 **end**
// **Stage III - Prediction**
18 **begin**
19 $labels \leftarrow$ Classify$\left(\mathbf{F}, \mathbf{Z}_{opt}, \mathbf{F}_{test}\right)$
20 **forall the** $i \in [1, \mathrm{N}]$ **do**
21 Distance$\left(\mathbf{Z}_{opt}, \mathbf{F}\right)$
22 **end**
23 $labels \leftarrow$ Sort$\left(\text{Distance}\left(\mathbf{Z}_{opt}, \mathbf{F}\right)\right)$
24 **return** $labels$
25 **end**

Algorithm 1: Pseudocode - Proposed Approach

Input: $\mathbf{F} = \{f_n\}_{n=1}^{N} \in \mathbb{R}^{\mathrm{N}\times\mathrm{P}}$, $\mathbf{Q} \in \mathbb{R}^{\mathrm{P}\times\mathrm{K}}$, β_1, β_2
Output: Dictionary, atom indices and coefficients
15.1 $\mathbf{R}_0 \leftarrow \mathbf{W}, dictIdx \leftarrow \phi$
15.2 **while** $\mathbf{R}_0 \rightarrow 0$ **do**
15.3 $t \leftarrow 0$ Select $z_k \in \mathbf{Z}$, such that

$$\min_{\mathbf{Q},\mathbf{Z}} \left[\beta_2 \sum_{n=1}^{\mathrm{N}} ||f_n - q_n\mathbf{Z}||^2 + \beta_1 \sum_{n=1}^{\mathrm{N}} |q_n|_1 + G\left(\mathbf{Q}\right) \right], \quad \text{subject to } |q_n| \leqslant 1,\ \forall n = 1, 2, ..., N$$

15.4 $dictIdx \leftarrow dictIdx \cup k$
// Projection and residual
15.5 $\mathbf{O}_t \leftarrow \mathbf{Q} * inv\left(\mathbf{Q}^T * \mathbf{Q}\right) * \mathbf{Q}^T$
15.6 $\mathbf{R}_t \leftarrow \mathbf{F} - \mathbf{O}_t\,\mathbf{F}$
15.7 $t \leftarrow t + 1$
15.8 **end**
15.9 **return** $\mathbf{Q}, \mathbf{Z}$, *dictIdx*

Algorithm 2: Pseudocode - SAD Module

TABLE III: Confusion Matrix - Material Discrimination

	Sand	**Plastic**	**Metal**
Sand	**0.9721**	0.0144	0.0133
Plastic	0.0151	**0.9823**	0.0024
Metal	0.0140	0.0035	**0.98239**

TABLE IV: Confusion Matrix - Mine Discrimination

	Plastic 1	**Plastic 2**	**Metal 1**	**Metal 2**	**Sand**
Plastic 1	**0.9755**	0	0.0020	0	0.0224
Plastic 2	0.0054	**0.9905**	0.0007	0.0020	0.0014
Metal 1	0.0014	0.0027	**0.9946**	0	0.0014
Metal 2	0.0014	0.0068	0	**0.9891**	0.0027
Sand	0.0102	0.0007	0	0.0007	**0.9884**

TABLE V: Effect of *Depth Representation* (DR) on accuracy

	Plastic 1	**Plastic 2**	**Metal 1**	**Metal 2**
Without DR(%)	92.65	95.65	97.62	98.10
With DR(%)	**97.55**	**99.05**	**99.46**	**98.91**

A. Experiment 1 - Material Discrimination

The confusion matrix for material discrimination is shown in Table III. A subset of 8520 target signatures, equally divided into three different materials was selected. A 10-fold cross-validation classification was then performed using the proposed approach resulting in a mean classification error rate of $\mathbf{0.021}\%$.

B. Experiment 2 - Mine Discrimination

The aim of this experiment was to seek answers for the following questions: i) can mines with structural variation but similar spectral signatures be classified correctly?, and, ii) what impact do the *Geometric* features, Section II-A2, have on classification? Table IV lists the confusion matrix for mine classification when geometric properties are included, using the full SDR representation, Eq. 2. A subset of 7350 target signatures, equally divided into five different classes was selected. The mean classification error rose by $\uparrow \mathbf{3.6}\%$ when geometry based DR was neglected. The effect on accuracy of classification for four different mines with and without DR is listed in Table V. Figure 5 illustrates the learnt coefficients, $\mathbf{Q}$, clustered into different mine types. The 3D point cloud, shown within, is segmented not only on the basis of their spectral content but also their geometric features. For illustration purposes, the clusters are plotted along three dimensions, area-under-curve, A_λ, sphericity, $S_\mathcal{E}$ and linearity, $L_\mathcal{E}$, respectively.

V. Conclusion

A novel spectral-depth representation is presented that is highly discriminatory in characterising different target signatures underwater. A custom-made realistically scaled exemplar with known and unknown targets has been investigated using a multi-spectral single photon counting LiDAR system. Multi-spectral measurements were made underwater on targets with

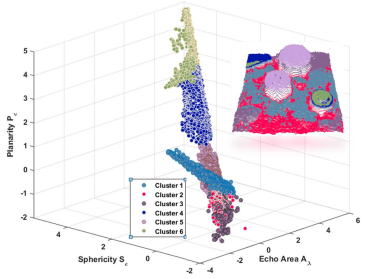

Fig. 5: Mine clusters using the spectral depth codes, $\mathbf{Q}$, on the spectral axis, echo area; and the depth axis, linearity and sphericity, respectively.

different shapes and materials, Section I-B. Using the proposed spectral depth representation sparse codes are optimised for maximum discrimination between different materials and mines, demonstrating accuracies of $\mathbf{97.8}\%$ and $\mathbf{98.7}\%$, respectively. Combining depth with spectral data, the approach is very effective at discriminating targets of different shapes, but with similar spectral response, or conversely of similar shape but having different spectra. When spectral features alone are considered, the discrimination error reported for Plastic 1 mine is 7.35%. But, when spectral and depth representation is considered, the error reduces to $\mathbf{2.45}\%$, Table V. This work has been the first to report the analysis and discrimination of multi-spectral underwater single photon counting LiDAR signals as an alternative to acoustic MCM.

Acknowledgment

This work was supported by the Engineering and Physical Sciences Research Council (EPSRC) under Grant EP/K014277/1 and the MOD University Defence Research Collaboration in Signal Processing.

References

[1] L. Guo, N. Chehata, C. Mallet, and S. Boukir, "Relevance of airborne lidar and multispectral image data for urban scene classification using random forests," *ISPRS Journal of Photogrammetry and Remote Sensing*, vol. 66, no. 1, pp. 56–66, 2011.

[2] A. G. Cottin, D. L. Forbes, and B. F. Long, "Shallow seabed mapping and classification using waveform analysis and bathymetry from shoals lidar data," *Canadian Journal of Remote Sensing*, vol. 35, no. 5, pp. 422–434, 2009.

[3] P. S. Chhabra, A. M. Wallace, and J. R. Hopgood, "Anomaly detection in clutter using spectrally enhanced ladar," in *SPIE Defense+ Security*, pp. 946508–946508, International Society for Optics and Photonics, 2015.

[4] J. C. Fernandez-Diaz, W. E. Carter, R. L. Shrestha, and C. L. Glennie, "Now you see it now you dont: Understanding airborne mapping lidar collection and data product generation for archaeological research in mesoamerica," *Remote Sensing*, vol. 6, no. 10, pp. 9951–10001, 2014.

[5] A. Maccarone, A. McCarthy, X. Ren, R. E. Warburton, A. M. Wallace, J. Moffat, Y. Petillot, and G. S. Buller, "Underwater depth imaging using time-correlated single-photon counting," *Optics Express*, vol. 23, no. 26, pp. 33911–33926, 2015.

[6] K. F. West, B. N. Webb, J. R. Lersch, S. Pothier, J. M. Triscari, and A. E. Iverson, "Context-driven automated target detection in 3d data," in *Defense and Security*, pp. 133–143, International Society for Optics and Photonics, 2004.

[7] G. Csurka, C. Dance, L. Fan, J. Willamowski, and C. Bray, "Visual categorization with bags of keypoints," in *Workshop on statistical learning in computer vision, ECCV*, vol. 1, pp. 1–2, Prague, 2004.

[8] J. A. Tropp, A. C. Gilbert, and M. J. Strauss, "Algorithms for simultaneous sparse approximation. part i: Greedy pursuit," *Signal Processing*, vol. 86, no. 3, pp. 572–588, 2006.